

# Prospects for assembling ultracold radioactive molecules from laser-cooled atoms

Jacek Klos,<sup>1,2</sup> Hui Li,<sup>1</sup> Eite Tiesinga,<sup>2</sup> and Svetlana Kotochigova<sup>1,\*</sup>

<sup>1</sup>*Department of Physics, Temple University, Philadelphia, Pennsylvania 19122, USA*

<sup>2</sup>*Joint Quantum Institute, National Institute of Standards and Technology  
and University of Maryland, Gaithersburg, Maryland 20899, USA*

(Dated: December 1, 2021)

Molecules with unstable isotopes often contain heavy and deformed nuclei and thus possess a high sensitivity to parity-violating effects, such as Schiff moments. Currently the best limits on Schiff moments are set with diamagnetic atoms. Polar molecules with quantum-enhanced sensing capabilities, however, can offer better sensitivity. In this work, we consider the prototypical  $^{223}\text{Fr}^{107}\text{Ag}$  molecule, as the octupole deformation of the unstable  $^{223}\text{Fr}$  francium nucleus amplifies the nuclear Schiff moment of the molecule by two orders of magnitude relative to that of spherical nuclei and as the silver atom has a large electronegativity. To develop a competitive experimental platform based on molecular quantum systems,  $^{223}\text{Fr}$  atoms and  $^{107}\text{Ag}$  atoms have to be brought together at ultracold temperatures. That is, we explore the prospects of forming  $^{223}\text{Fr}^{107}\text{Ag}$  from laser-cooled Fr and Ag atoms. We have performed fully relativistic electronic-structure calculations of ground and excited states of FrAg that account for the strong spin-dependent relativistic effects of Fr and the strong ionic bond to Ag. In addition, we predict the nearest-neighbor densities of magnetic-field Feshbach resonances in ultracold  $^{223}\text{Fr}+^{107}\text{Ag}$  collisions with coupled-channel calculations. These resonances can be used for magneto-association into ultracold, weakly-bound FrAg. We also determine the conditions for creating  $^{223}\text{Fr}^{107}\text{Ag}$  molecules in their absolute ground state from these weakly-bound dimers via stimulated Raman adiabatic passage using our calculations of the relativistic transition electronic dipole moments.

## I. INTRODUCTION

Engineered quantum matter holds promise for quantum computation as well as the development of novel materials and sensors. Quantum technologies based on atoms and atomic ions have partly fulfilled these promises [1–4]. Ultracold, sub-millikelvin molecules represent a next frontier for controlling quantum matter. The richness of their internal states has established molecules as promising precision-measurement tools in quantum science, assisted by long coherence times among internal states in laser-based optical traps [5–7]. Key to these advances has been the development of cooling techniques, which sufficiently reduce the entropy of the molecules in order to apply ever more refined quantum control techniques.

Advancing fundamental physics and related precision measurements often require the creation of unexplored polar molecules [8]. Current efforts in this direction focus on sensors of fundamental interactions and forces using cold and ultracold molecules [9, 10]. Here, the search for forces that violate both time-reversal (T) and parity (P) invariance is of fundamental importance for physics beyond the standard model. P,T-odd nuclear interactions, for example, give rise to the nuclear Schiff moment [11], which may interact with the electrons in the molecule and lead to measurable shifts in molecular spectra [12].

Among the candidates for measurements of the nuclear Schiff moment are molecules containing unstable isotopes of radium (Ra) and francium (Fr), which have

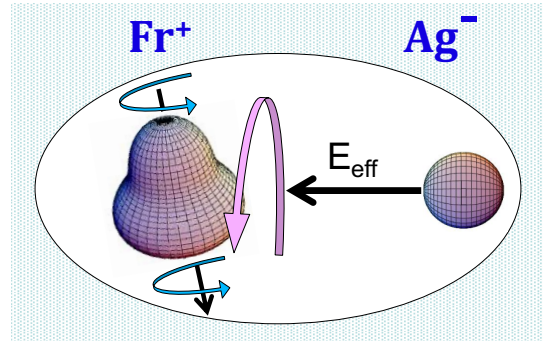


FIG. 1. Beyond-standard-model quantum sensor based on FrAg molecules containing unstable Fr with a deformed non-spherical nucleus. The strong ionic bond of FrAg leads to a strong internal electric field  $\mathcal{E}_{\text{eff}}$  significantly enhancing the sensitivity to parity-violating effects.

an octupole-deformed nucleus and thus possess a high sensitivity to parity violation [13–18]. Both heavy atom species are now routinely cooled and trapped in magneto-optical traps despite their short lifetime by either  $\alpha$  or  $\beta$  decay [19, 20]. In the search for bonding partners for Ra and Fr two criteria must be considered: *i*) bonding partners must have a large electron affinity that leads to an ionic bond and a strongly polarized Ra or Fr atom; *ii*) being amenable to laser cooling and trapping. An ionic bond is also correlated with a large permanent molecular electronic dipole moment and with a large effective electric field,  $\mathcal{E}_{\text{eff}}$ , acting on either the unstable nucleus or the electrons [8, 18, 21]. Among the most relevant partner for both Ra and Fr is the silver (Ag) atom [18, 22]. It satisfies both criteria as having a large electronegativity

\* skotoch@temple.edu

of  $hc \times 10521 \text{ cm}^{-1}$  [23], and having been laser cooled [24]. Here,  $h$  is the Planck constant and  $c$  is the speed of light in vacuum.

In this paper, we consider the prototypical francium-silver molecule FrAg, shown in Figure 1 for the development of a quantum sensor in search of a nuclear Schiff moment. The idea is to assemble FrAg molecules from laser-cooled  $^{223}\text{Fr}$  and  $^{107}\text{Ag}$  atoms [22]. Both atoms have an electron-spin-1/2 or  $^2\text{S}$  electronic ground state, while their electronic molecular ground state is well described as an electron-spin-zero or singlet  $^1\Sigma^+$  Hund's case (a) state [25, 26], similar to that for the ground state of bi-alkali-metal molecules. Alkali-metal dimers have already been assembled from ultra-cold atoms and been shown to be scientifically relevant [27, 28].

We first assume that the ultracold atoms are prepared in their energetically lowest Zeeman, hyperfine state and collide in the presence of an external magnetic field and from there can be bound together with a small binding energy of order  $hc \times 10^{-3} \text{ cm}^{-1}$ , in an electronic configuration that is predominantly of triplet  $a^3\Sigma^+$  character. This binding process is either achieved via a slow time-dependent sweep or ramp of the magnetic field near a Fano-Feshbach resonance, also known as magneto-association, or via microwave radiation near such resonances [29]. We will show that useable Feshbach resonances exist in  $^{223}\text{Fr}$  and  $^{107}\text{Ag}$  collisions.

The next step is to search for a route, based on stimulated Raman adiabatic passage (STIRAP) processes [30], to coherently transfer the population from a weakly-bound rovibrational state to the strongly-bound rovibrational ground state of the  $X^1\Sigma^+$  state via a rovibrational state of the mixed and coupled  $b^3\Pi$  and  $A^1\Sigma^+$  excited electronic states. Mixing is due to relativistic spin-orbit interactions, which requires us to label electronic state with the Hund's case (c) coupling scheme rather than the case(a) scheme so far [25, 26].

The two-step formation of ultracold FrAg molecules from ultracold Fr and Ag is made challenging due to a lack of knowledge of their relativistic electronic, rovibrational, and hyperfine structure in both electronic ground and excited states. To our knowledge, only the electronic singlet and triplet ground-state potentials of FrAg have been calculated [31]. Here, we describe our theoretical study of potentials, electric dipole moments, and rovibrational states of FrAg. In addition, this includes the prediction of Feshbach resonance densities and locations, as well as the development of Raman schemes for the formation of the absolute ground state of FrAg. Unless otherwise noted, we present results for rovibrational states of the  $^{223}\text{Fr}^{107}\text{Ag}$  isotopologue.

TABLE I. Spectroscopic constants of  $^{223}\text{Fr}^{107}\text{Ag}$  in relativistic ground and excited states relevant to the STIRAP scheme. These include equilibrium interatomic separation  $R_e$ , dissociation energy  $D_e$ , harmonic spring constant  $k$ , harmonic (angular) frequency  $\omega_e$ , and rotational constant  $B_e$ . Data is compared to the non-relativistic results of Ref. [31] where available.

State	$R_e/a_0$	$D_e/hc$ ( $\text{cm}^{-1}$ )	$k/hc$ ( $\text{cm}^{-1}/a_0^2$ )	$\omega_e/2\pi c$ ( $\text{cm}^{-1}$ )	$B_e/hc$ ( $\text{cm}^{-1}$ )
1(0 <sup>+</sup> )	6.164	12635	4391.5	85.54	0.0219
Non-rel. [31]	6.190	12700	-	84.2	0.0215
1(0 <sup>-</sup> )	9.422	205	68.942	10.72	0.0094
Non-rel. [31]	9.451	193	-	10.6	0.0093
2(0 <sup>+</sup> )	9.100	4017	342.18	23.88	0.0010
3(0 <sup>+</sup> )	6.740	8125	2093.2	59.06	0.0183

## II. RESULTS

### A. Electronic potentials and transition dipole moments

We begin with the determination of the adiabatic potential energy surfaces of FrAg electronic states as well as transition electronic dipole moments between these states as functions of atom-atom separation  $R$ . Here, relativistic electronic structure calculations using the DIRAC computational suite [32] enable us to account for spin-orbit effects on FrAg states. This includes spin-orbit coupling between the  $A^1\Sigma^+$  and  $b^3\Pi$  states as well as the weaker second-order spin-orbit splitting of the  $a^3\Sigma^+$  state.

Adiabatic potentials are uniquely labeled by  $n(\Omega^\sigma)$  within the Hund's case (c) notation, where  $\Omega$  is the absolute value of the projection of the total electronic angular momentum on the internuclear axis and  $\sigma = \pm$  represents the even or odd reflection symmetry of the electron wavefunction through a plane containing the internuclear axis when  $\Omega = 0$ . Finally,  $n = 1, 2, \dots$  labels states of the same  $\Omega^\sigma$  value ordered by increasing energy. Then, the energetically-lowest  $n(\Omega^\sigma) = 1(0^+)$  state connects to the Hund's-case-(a)  $X^1\Sigma^+$  state while the  $a^3\Sigma^+$  state has  $1(0^-)$  and  $1(1)$  components. The  $A^1\Sigma^+$  and  $b^3\Pi$  states mix to form  $\Omega^\sigma = 0^+, 0^-, 1$ , and  $2$  states, but in this article we will mostly be interested in the  $2(0^+)$  and  $3(0^+)$  states. We also determine the  $R$ -dependent transition dipole moments between  $n(\Omega^\sigma)$  ground and excited states. A description of electron orbitals used in the DIRAC calculations and values for the long-range van-der-Waals and other dispersion coefficients can be found in Appendix A.

Figure 2 shows our results for electronic relativistic adiabatic potentials  $V_{n(\Omega^\sigma)}(R)$  relevant for transferring population from weakly-bound Feshbach molecular states to the absolute rovibrational ground state of the  $1(0^+)$  potential. In the figure atom separations are expressed

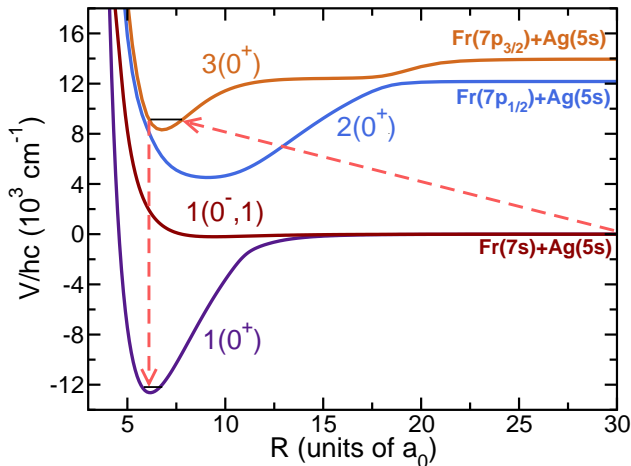


FIG. 2. Relevant electronic potentials of FrAg as functions of atomic separation  $R$ . Potentials are identified by Hund's case (c) state labels and for large separations by atomic states. The zero of energy is at the dissociation limit or threshold of the  $1(0^+)$  and  $1(0^-, 1)$  states. The small splitting between the  $1(0^-)$  and  $1(1)$  states is invisible on the scale of this figure. Short black lines in the  $1(0^+)$  and  $3(0^+)$  potentials indicate rovibrational levels of these potentials. The dashed lines with arrows connecting these levels with near threshold bound states indicate a possible STIRAP pathway to the FrAg rovibrational ground state.

in units of  $a_0 = 0.05292$  nm, the Bohr radius. Spectroscopic constants for these potentials can be found in Table I, while a graph with additional excited electronic potentials can be found in Appendix A. The dissociation energy of our  $1(0^+)$  potential is only 0.5% smaller than that of Ref. [31] based on non-relativistic calculations. The corresponding fractional difference for the shallow  $1(0^-)$  potential is about 10%. The absolute difference, however, is only  $hc \times 12$   $\text{cm}^{-1}$ . There is also noticeable difference in their harmonic constant  $\omega_e$ ,  $hc \times 85.5$   $\text{cm}^{-1}$  for relativistic potential versus  $hc \times 84.2$   $\text{cm}^{-1}$  for non-relativistic potential.

At first glance, there is similarity with the potential surfaces for heavy di-atomic alkali-metal molecules. This is due to the single active open valence orbital of alkali-metal and silver atoms. Thus we find a deep  $1(0^+)$  ground state and shallow nearly-degenerate  $1(0^-)$  and  $1(1)$  excited states that correlate to the non-relativistic Hund's case (a)-like  $X^1\Sigma^+$  and  $a^3\Sigma^+$  states, respectively. These states dissociate to two  $^2S$  ground-state atoms. Next, we observe the avoided crossings between the  $2(0^+)$  and  $3(0^+)$  levels that dissociate to an excited  $^2P_{j=1/2}$  or  $^2P_{j=3/2}$  Fr atom and a ground-state Ag atom. For alkali-metal dimers these states also exist. The two states are the result of spin-orbit mixing of the non-relativistic  $A^1\Sigma^+$  and  $b^3\Pi$  states. Near avoided crossings the potentials for these non-relativistic states cross.

There are significant differences between the potentials of FrAg and alkali-metal dimers as well. First, the ground

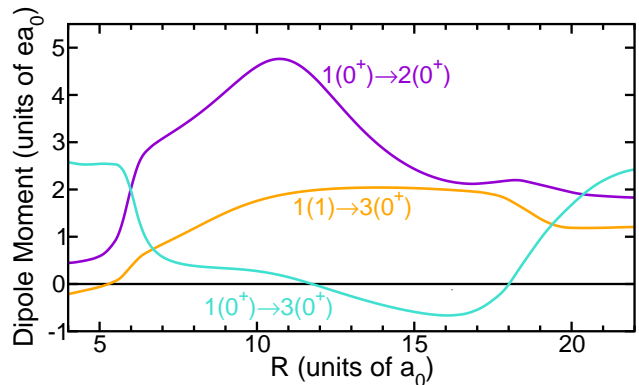


FIG. 3. Relevant electronic transition dipole moments  $d$  of FrAg as functions of separation  $R$ . The moments have been found from relativistic calculations. The purple, turquoise, and orange curves are for the  $1(0^+) \rightarrow 2(0^+)$ ,  $1(0^+) \rightarrow 3(0^+)$ , and  $1(1) \rightarrow 3(0^+)$  transitions, respectively.

$1(0^+)$  potential for FrAg is more than twice as deep at its equilibrium separation as the corresponding potential of KRb [27], RbCs [33, 34], and Cs<sub>2</sub> [35]. The bond in FrAg is far more ionic. On the other hand, the depths of the shallow  $1(0^-, 1)$  states are very similar. Second, the shape of the excited  $2(0^+)$  and  $3(0^+)$  potentials differ in two important ways. The extended, flat minimum of the  $2(0^+)$  state between  $R = 8a_0$  and  $11a_0$  is seen to avoid with the  $1(0^+)$  state. In alkali-metal dimers, the harmonic (spring) constant near the equivalent minimum of the  $2(0^+)$  state is significantly larger and the avoided crossing with the  $X^1\Sigma^+$  potential much less pronounced. Finally, for FrAg the  $2(0^+)$  and  $3(0^+)$  potentials have an avoided crossing on their inner walls, where the slope of the potentials with respect to  $R$  is negative. For alkali-metal dimers this avoided crossing occurs for separations, where the slope of  $2(0^+)$  potential is already positive.

We have also determined electronic transition dipole moments between ground and excited electronic states. Computational details can be found in Appendix A. Three of these dipole moments as functions of internuclear separation  $R$  are shown in Fig. 3. First, we observe that dipole moments undergo rapid changes near  $6a_0$  and  $19a_0$  corresponding to the avoided crossings between the  $2(0^+)$  and  $3(0^+)$  potentials in Fig. 2. Second, we will mostly pay attention to the two transition dipole moments to the  $3(0^+)$  state. The dipole moments are large, of order  $ea_0$ , and are non-zero for most  $R$ . Here,  $e$  is the elementary charge. Especially noticeable is the large dipole moment at the asymptotic limit due to spin-orbit mixing of the  $7p_{1/2}$  and  $7p_{3/2}$  excited levels of Fr. As we will show, this promises efficient transfer from a weakly-bound  $1(1)$  molecule to the strongly-bound  $1(0^+)$  molecule.

For a precise description of ultra-cold Fr and Ag collisions, we need the splitting between the  $1(0^-)$  and  $1(1)$  components of the  $a^3\Sigma^+$  potential. This is the second-order spin-orbit interaction and is shown in Fig. 4. Its

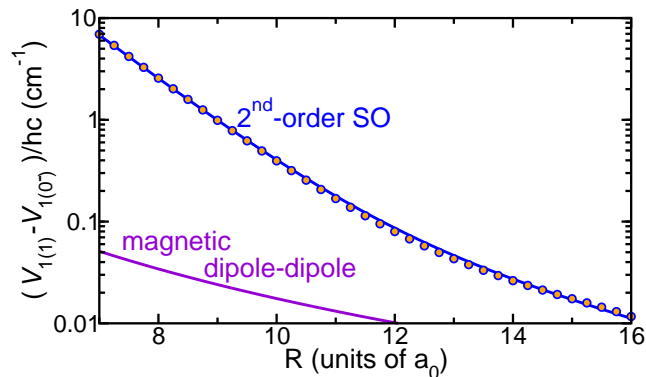


FIG. 4. The second-order spin-orbit splitting (filled blue circles) of FrAg, defined as the potential energy of the  $\Omega = 1$  component minus that of the  $\Omega = 0^-$  component of the  $a^3\Sigma^+$  state, as a function of interatomic separation  $R$  based on relativistic electronic-structure calculations. The blue curve is a fit to this data using the functional form given in the text. The purple curve shows *minus* the corresponding splitting from the magnetic dipole-dipole interaction due to the magnetic moments of the electrons.

behavior is determined by the overlap of electron wavefunctions from each atom and, thus, decreases exponentially with increasing separation  $R$ . For later use, the data has been fit to

$$V_{1(1)}(R) - V_{1(0^-)}(R) = A_1 e^{-B_1(R-R_1)} + A_2 e^{-B_2(R-R_2)}, \quad (1)$$

where  $A_1/hc = 2.35824 \text{ cm}^{-1}$ ,  $B_1 = 1.01701 a_0^{-1}$ ,  $R_1 = 8a_0$  and  $A_2/hc = 0.022 \text{ cm}^{-1}$ ,  $B_2 = 0.37 a_0^{-1}$ ,  $R_2 = 14a_0$ . For later use we define the singlet  $X^1\Sigma^+$  potential  $V_X(R) \equiv V_{1(0^+)}(R)$  and triplet  $a^3\Sigma^+$  potential  $V_a(R) = (V_{1(0^-)}(R) + 2V_{1(1)}(R))/3$  (See also App. A.)

A comparison of the 2<sup>nd</sup>-order spin-orbit interaction of FrAg with that of heavy alkali-metal dimers, such as RbCs [34], shows that the former is almost ten times stronger at the inner-turning point of the  $a^3\Sigma^+$  potential near  $8a_0$  when the potential energy is that of the dissociation limit or atom-atom threshold. In Fig. 4, we also show *minus* the splitting between  $1(1)$  and  $1(0^-)$  due to the magnetic dipole-dipole interaction between the magnetic moments of electron spins of Fr and Ag. This dipole-dipole interaction is of order  $E_h a_0^3 \alpha^2 / R^3$ , where  $E_h$  is the Hartree energy and  $\alpha$  is the fine-structure constant. It is small for the separations shown in the figure, but will dominate for  $R > 20a_0$ .

### B. Magnetic Feshbach resonances in ultracold Fr+Ag collisions

We can now describe results for ultra-cold,  $\mu\text{K}$  collisions of  $^{223}\text{Fr}$  and  $^{107}\text{Ag}$  in their  $^2\text{S}$  electronic ground state as well as the near-threshold, weakly-bound rovibrational states of  $^{223}\text{Fr}^{107}\text{Ag}$ . Specifically, we describe collisional magnetic Feshbach resonances when

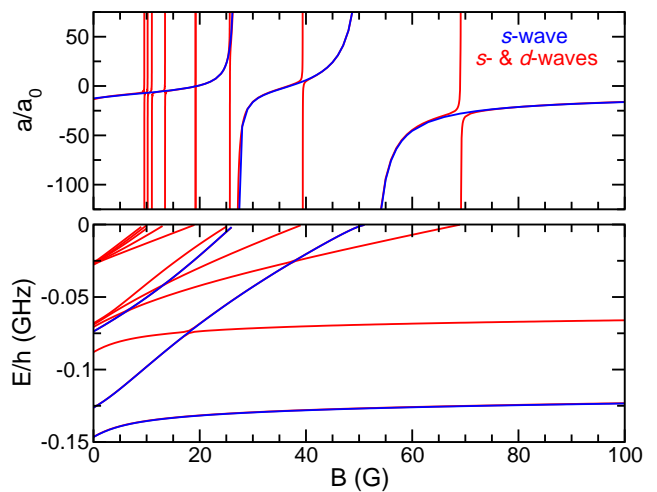


FIG. 5. Scattering length,  $a$ , (top panel) for colliding  $^{223}\text{Fr}$  and  $^{107}\text{Ag}$  atoms in their energetically-lowest hyperfine state and their near-threshold bound-state energies,  $E$ , (bottom panel) as functions of magnetic field  $B$  up to 100 G. Blue and red curves correspond to calculations including channels with only  $\ell = 0$  ( $s$ -) and  $\ell = 0, 2$  ( $s$ -,  $d$ -) partial waves, respectively.

these atoms are prepared in their energetically-lowest electronic, hyperfine, and Zeeman states in the presence of an external magnetic field with strength  $B$ . These resonances are due to mixing of the  $R$ -dependent molecular interactions by the Zeeman and hyperfine or Fermi-contact interactions of the  $^2\text{S}$  atoms.

The Hamiltonian  $H$  for the relative motion of  $^{223}\text{Fr}$  and  $^{107}\text{Ag}$  is similar to that of interacting ground-state hydrogen atoms or alkali-metal atoms. Following Ref. [36], the atoms are assumed to be point-like with a mass equal to that of the atoms. Each atom has an electron spin (quantum number) equal to  $1/2$  and a non-zero nuclear spin, whose value is unique to the actual isotope. Here,  $^{223}\text{Fr}$  has nuclear spin  $3/2$  and  $^{107}\text{Ag}$  has nuclear spin  $1/2$ . Electron and nuclear spin of each atom are coupled by the Fermi-contact and Zeeman interactions. Relevant hyperfine constants,  $g$  factors, and masses, are taken from Refs. [37–41], where  $^{107}\text{Ag}$  has an “inverted” hyperfine structure. The Fermi-contact coefficient of  $^{223}\text{Fr}$  is many times larger than the absolute value of that of  $^{107}\text{Ag}$ .

The Hamiltonian also contains the relative kinetic energy operator, which is an operator in the separation between the two atoms  $R$  and the orientation of their interatomic axis  $\hat{R}$ . Eigenfunctions of the orientation-dependent part of the kinetic energy operator are spherical harmonic functions in  $\hat{R}$  labeled by orbital angular momentum or partial wave  $\ell$  and its projection  $m_\ell$  along the magnetic field direction. In addition,  $H$  includes isotropic molecular interactions that only depend on separation  $R$ . The isotropic potential for total molecular electron spin zero is  $V_X(R)$ , while that for total electron spin one is  $V_a(R)$  as defined in the previous subsection. Finally, the Hamiltonian contains the weak 2<sup>nd</sup>-



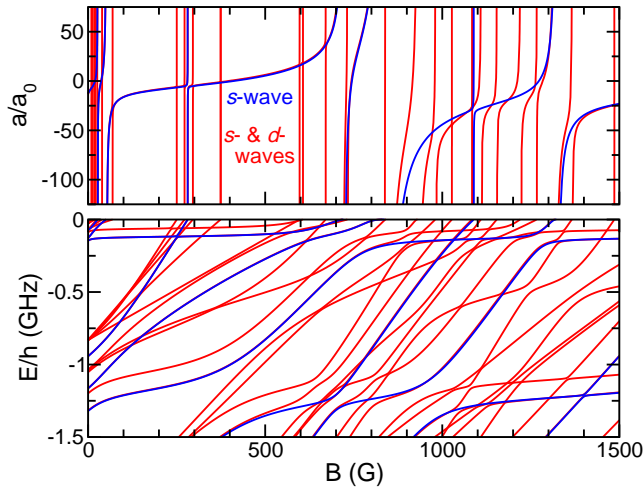


FIG. 6. Scattering length,  $a$ , (top panel) and near-threshold bound-state energies,  $E$ , (bottom panel) of  $^{223}\text{Fr}+^{107}\text{Ag}$  as functions of magnetic field  $B$  up to 1500 G. Other conditions, parameters, and definitions of line styles are as in Fig. 5.

order spin-orbit and magnetic dipole-dipole interactions. They are anisotropic, depend on the orientation of the total electron spin relative to  $\hat{R}$ , and lift the  $1(0^-)$  and  $1(1)$  degeneracy. These weaker interactions mix molecular states with even  $\ell$  (that is the  $s, d, \dots$  partial waves for  $\ell = 0, 2, \dots$ ) or odd  $\ell$  (that is the  $p, f, \dots$  partial waves).

We have computed the  $s$ -wave scattering length,  $a$ , as a function of magnetic field, a Feshbach resonance spectrum [29], for ultracold  $^{223}\text{Fr}+^{107}\text{Ag}$  collisions. For the calculations, we rely on the coupled-channels method using our potential energy surfaces. The scattering length is determined from elastic  $s$ -wave scattering amplitudes at a collision energy of  $k \times 1 \mu\text{K}$  with entrance channel where  $^{223}\text{Fr}$  and  $^{107}\text{Ag}$  are in their energetically-lowest  $m_{\text{Fr}} = +1$  and  $m_{\text{Ag}} = -1$  hyperfine state, respectively. Here,  $m_X$  with  $X = \text{Fr}$  and  $\text{Ag}$  are projections of the atomic angular momentum along the  $B$ -field direction and  $k$  is the Boltzmann constant. For the calculations, allowed molecular coupled channels have conserved projection  $M_{\text{tot}} = m_{\text{Fr}} + m_{\text{Ag}} + m_\ell = 0$  along the  $B$ -field direction and even values of  $\ell$ . For  $^{223}\text{Fr}+^{107}\text{Ag}$  with  $M_{\text{tot}} = 0$ , there are eight  $\ell = 0$  channels and thirty  $\ell = 2$  channels. In addition, we have determined the Zeeman, hyperfine, rotation and vibration resolved near-threshold bound states with  $M_{\text{tot}} = 0$ .

Figures 5 and 6 show our computed scattering lengths  $a(B)$  and threshold bound-state energies  $E(B)$  relative to the entrance channel energy as function of magnetic field strength  $B$  up to 1500 G. Here, 1 G equals 0.1 mT. The figures show results from calculations that include only  $\ell = 0$  channels as well as those that include all  $\ell = 0$  and 2 channels. In both cases the scattering length has resonances, where its value rapidly goes through  $\pm\infty$  with  $B$ . The values for  $a$  are mostly identical away from resonances for the two cases. In fact, the positions and

(magnetic) widths of those resonances found in both  $s$ -wave channel and  $s, d$ -wave channel calculations agree to a fraction of a Gauss. These resonances are  $s$ -wave Feshbach resonances, while the remaining resonances are  $d$ -wave resonances. Between 0 G and 1500 G, we find seven  $s$ -wave and just over 30  $d$ -wave Feshbach resonances.

Our analysis also implies that the anisotropic interactions, coupling  $s$ - and  $d$ -wave channels, are weak. With some exceptions, the magnetic widths of  $d$ -wave resonances are smaller or narrower than those for  $s$ -wave resonances. Adding larger partial-wave channels, that is  $\ell = 4, 6, \dots$ , to the calculations will create even-narrower resonances.

A comparison of the top and bottom panels in Figs. 5 and 6 shows that a resonance in  $a(B)$  always corresponds to a threshold bound state with zero binding energy. Each of these zero-energy bound states can be followed back to a bound state at zero magnetic field, where a resonance that occurs at larger  $B$  has a larger binding energy at 0 G. For example, zero-energy bound states that occur around  $B = 1000$  G have a zero-field binding energy of  $\approx h \times 5$  GHz, outside the range of energies shown in Fig. 6. Moreover, the magnetic moments of the bound states,  $-dE/dB$ , are related to the magnetic moments of closed channels, *i.e.* atom-pair channels with energies that are larger than that of the entrance channel. These closed channels have magnetic moments of up to a few times the Bohr magneton  $\mu_B$  with  $\mu_B/h \approx 1.40$  MHz/G relative to that of the entrance channel.

Further analysis of the near-threshold bound state wavefunctions has shown that they originate from coupling among the last three  $s$ - and  $d$ -wave bound states, labeled  $v = -1, -2, -3$ , respectively, of the  $V_X(R)$  and  $V_a(R)$  potentials. In fact, bound states with  $-0.2 \text{ GHz} < E/h < 0 \text{ GHz}$  have at least 80% of their wavefunctions combined in the  $1(0^-)$  and  $1(1)$  states. These observations are consistent with the energy-level density expected from the identical attractive long-range  $-C_6/R^6$  van-der-Waals tail of the two potentials. Analytical analysis of bound state energies of a van-der-Waals potential by Gao in Ref. [42] shows that for the  $C_6$  coefficient of  $\text{FrAg}$  the relations  $-5.1 \text{ GHz} \leq E_{v=-3}/h \leq -1.6 \text{ GHz} \leq E_{v=-2}/h \leq -0.23 \text{ GHz} \leq E_{v=-1}/h < 0 \text{ GHz}$  hold, where  $E_{v=-3, -2, -1}$  are the energies of the last three bound states. For a  $d$ -wave channel the energy intervals satisfy  $-7.7 \text{ GHz} \leq E_{v=-3}/h \leq -2.8 \text{ GHz} \leq E_{v=-2}/h \leq -0.60 \text{ GHz} \leq E_{v=-1}/h < 0 \text{ GHz}$ . Combined with the number of closed  $s$ - and  $d$ -wave channels and their threshold energies this leads to the energy level density seen in Figs. 5 and 6.

Finally, we note that our calculations of our relativistic potentials are not exact. In fact, based on electronic-structure calculations using smaller basis sets, we conclude that the number of bound states has an uncertainty of at least two and one for  $V_X(R)$  and  $V_a(R)$ , respectively. This implies that Figs. 5 and 6 only show a typical Feshbach spectrum. The resonance density in  $a(B)$ , however, will remain the same for any potential pair as the  $C_6$

coefficient for FrAg is sufficiently accurate. In fact, the density is  $0.005 \text{ G}^{-1}$  for  $s$ -wave resonances and  $0.02 \text{ G}^{-1}$  for  $d$ -wave resonances. The precise locations of Feshbach resonances are unknown. Finally, for the Feshbach spectrum in Figs. 5 and 6 the background scattering length away from resonances is negative. Changing the shape of the potentials can lead to a positive value for  $a$ . Reference [43] showed that for a van-der-Waals potential there is a 75 % chance of a positive scattering length  $a$ . Joint experimental and theoretical studies of FrAg are required for determining the exact locations of magnetic Feshbach resonances.

### C. Formation of ultracold FrAg molecules by STIRAP

In this subsection, we derive initial guidelines for the formation of ultracold ground-state FrAg molecules by analyzing transition dipole moments between the initial, intermediate, and final molecular rovibrational states in stimulated Raman or STIRAP processes based on the pathway shown in Fig. 2. We can assume that FrAg molecules are first created in a weakly-bound near-threshold  $s$ -wave vibrational state by a slow ramp of the magnetic field through one of the  $s$ -wave Feshbach resonances found in the previous subsection. Such ramps are nearly 100 % efficient [29].

For our initial analysis of the stimulated Raman or STIRAP process we make several simplifying assumptions. First, we do not include the hyperfine and magnetic Zeeman interactions in the description of the weakly-bound  $s$ -wave vibrational states. Based on the realization that the wavefunctions of these bound states have at least an 80 % character in the  $a^3\Sigma^+$  state, it is reasonable to assume that the Raman process starts in either the  $v = -1, -2$ , or  $-3$   $s$ -wave vibrational level of the  $1(1)$  component of the  $a^3\Sigma^+$  state.

In the STIRAP-based formation of ultracold alkali-metal dimers [27, 28], the intermediate states were deeply-bound  $v', J' = 1$  ro-vibrational levels of  $n(\Omega^\sigma) = n(0^+)$  excited states with  $n = 2$  and 3. We will do so for FrAg as well, but introduce one additional approximation. We ignore non-adiabatic mixing near avoided crossings between the  $2(0^+)$  and  $3(0^+)$  states and focus on the  $3(0^+)$  state as the location of and harmonic frequency near its potential minimum are closer to that of the  $1(0^+)$  electronic ground-state potential. The final state in the STIRAP process is energetically lowest  $v = 0$ ,  $s$ -wave level of the  $1(0^+)$  state. (As an aside, note that the electronic dipole moments between the  $1(0^-)$  component of the  $a^3\Sigma^+$  state and  $n(0^+)$  states are strictly zero.)

The relevant quantities that are needed to evaluate the effectiveness of the upward and downward transitions in the STIRAP process are the vibrationally averaged

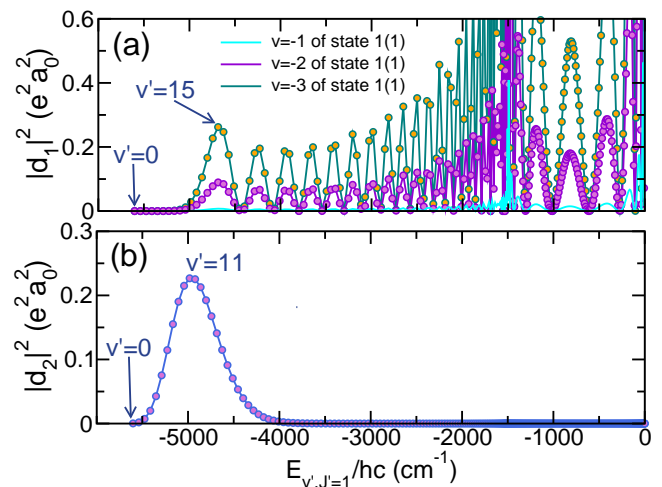


FIG. 7. Squared vibrationally averaged transition dipole moments of  $^{223}\text{Fr}^{107}\text{Ag}$  as functions of  $J' = 1$  vibrational binding energies  $E_{v',J'}$  of the  $3(0^+)$  excited state from the weakly bound  $s$ -wave  $v = -1, -2$ , or  $-3$  levels of the  $1(1)$  state (panel (a)) and from the most-deeply-bound  $s$ -wave vibrational level of the  $1(0^+)$  electronic ground state (panel (b)). These two types of transitions correspond to the upward and downward steps of the stimulated Raman process, respectively. Filled colored circles correspond bound states  $v'$  in the  $3(0^+)$  state. The  $v = -1$  data in panel (a) (cyan colored curve) are barely visible on the scale of the figure. The zero of energy for the  $x$  axis is at the  $\text{Fr}(7p_{3/2}) + \text{Ag}(5s)$  dissociation limit defined in Fig. 2,  $ea_0$  is the atomic unit for electric dipole moments, and  $e$  is the elementary charge.

dipole moments

$$d_{v',v}^{(\alpha,\beta)} = \int_0^\infty dR \phi_{v',J'=1}^{(\alpha)*}(R) d_{\alpha\beta}(R) \phi_{v,\ell=0}^{(\beta)}(R) \quad (2)$$

between electronic states  $\alpha = 3(0^+)$  and  $\beta = 1(0^+)$  or  $1(1)$ . Here,  $d_{\alpha\beta}(R)$  are electronic transition dipole moment shown in Fig. 3. The *radial* rovibrational wavefunctions  $\phi_{v',J'}^{(\alpha)}(R)$  and  $\phi_{v,\ell}^{(\beta)}(R)$  are unit-normalized and  $v = 0$  for  $\beta = 1(0^+)$  and  $v = -1, -2, -3$  for  $\beta = 1(1)$ . In principle, Eq. (2) must be multiplied by a dimensionless factor containing the photon polarization dependence [44]. They are always of the order of one and in view of our other approximation can be omitted.

The results of our calculation for the upward and downward transition dipole moments as functions of  $3(0^+)$   $J' = 1$  vibrational levels are shown in Figs. 7(a) and (b), respectively. For the upward transition in panel (a), we observe that the dipole moments are on the order of  $0.1ea_0$  for many of the vibrational levels  $v'$  of the  $3(0^+)$  state in the bottom half on the potential. For  $3(0^+)$  vibrational levels with energies near the  $\text{Fr}(7p_{1/2}) + \text{Ag}(5s)$  and  $\text{Fr}(7p_{3/2}) + \text{Ag}(5s)$  limits and thus with large, up to  $20a_0$ , radial extent the dipole moments are significantly larger. That is, the overlap of  $3(0^+)$  levels with the even-larger extended initial state is largest. Finally, we note that the size of the dipole moments increase with the

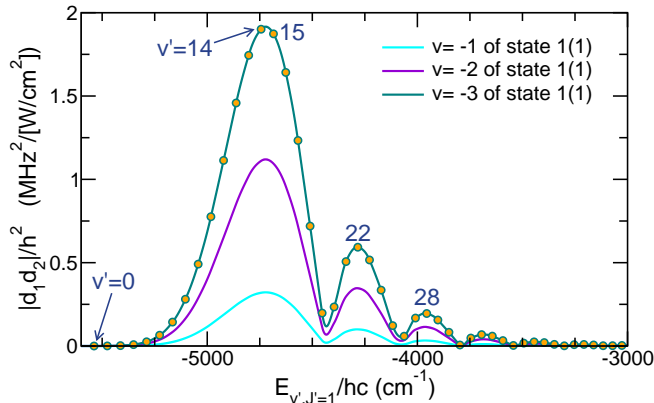


FIG. 8. Vibrationaly averaged two-photon transition dipole moments of  $^{223}\text{Fr}^{107}\text{Ag}$  for the stimulated Raman transition from weakly bound  $s$ -wave 1(1) vibrational levels  $v = -1, -2$ , and  $-3$  to the most-deeply-bound  $s$ -wave vibrational level of the  $1(0^+)$  electronic ground state as functions of  $J' = 1$  vibrational binding energies  $E_{v',J'=1}$  of the intermediate  $3(0^+)$  electronic state. The zero of energy for the  $x$  axis is at the  $\text{Fr}(7p_{3/2}) + \text{Ag}(5s)$  dissociation limit defined in Fig. 2. The data are derived from Fig. 7.

binding energy of the initial  $s$ -wave vibrational state  $v$ . Figure 7(b) shows the transition dipole moments for the downward step. Significant transition amplitudes only occurs for  $3(0^+)$  vibrational levels with an energy around  $hc \times 5000 \text{ cm}^{-1}$  below the  $\text{Fr}(7p_{3/2}) + \text{Ag}(5s)$  limit.

The transition amplitude for resonant two-photon, two color Raman transitions is the proportional to  $(d_1 \mathcal{E}_1)(d_2 \mathcal{E}_2)/(\Delta_{v',J'=1} + i\gamma_{v',J'=1})$ , where  $d_i$  and  $\mathcal{E}_i$  with  $i = 1$  or  $2$  are the vibrationaly averaged dipole moments and electric field strengths of the lasers for the upward and downward transitions, respectively. The frequencies  $\Delta_{v',J'=1}$  and  $\gamma_{v',J'=1}$  are the detuning from and the linewidth of rovibrational level  $v', J' = 1$  of the intermediate  $3(0^+)$  state, respectively. Figure 8 shows  $d_1 d_2$  for the last three 1(1)  $s$ -wave bound states as functions of vibrational energies of the  $3(0^+)$  potential. We see that the best candidates for intermediate state are vibrational levels  $v' = 14$  and  $v' = 15$ , about  $hc \times 1600 \text{ cm}^{-1}$  above the minimum energy of the  $3(0^+)$  potential. Starting from the  $v = -3$  vibrational level of the  $1(0^+)$  leads to the largest two-photon rates.

### III. CONCLUSION

Molecules with unstable isotopes often contain heavy and deformed nuclei and thus possess a high sensitivity to various parity-violating effects. In this paper, we theoretically studied the molecular properties of  $^{223}\text{Fr}^{107}\text{Ag}$ , a molecule with exceptional promise in quantum sensing and precision measurements of parity-violating effects. Experimental efforts will likely use molecules formed or associated from ultracold laser-cooled Fr and Ag atoms.

We therefore determined adiabatic relativistic electronic energies of ground and excited molecular states as well as electronic transition dipole moments between them and showed that it is feasible to create  $^{223}\text{Fr}^{107}\text{Ag}$  molecules by two-color photo-association or STIRAP to its energetically lowest rotational, vibrational state from ultracold  $^{223}\text{Fr}$  and  $^{107}\text{Ag}$  atoms.

To reach this conclusion, we set up a hyperfine- and Zeeman-resolved quantum coupled-channels scattering calculation for one microKelvin ground-state  $^{223}\text{Fr}$  and  $^{107}\text{Ag}$  atoms. From these calculations, we showed that many magnetic Feshbach resonances exist as a function of applied magnetic field up to 1500 G. We estimated that the nearest-neighbor level density of these resonances is  $0.005 \text{ G}^{-1}$  for  $s$ -wave resonances and  $0.02 \text{ G}^{-1}$  for  $d$ -wave resonances. We also found that the resonances are due to mixing of the last three, most weakly bound vibrational levels of the  $1(0^+)$  and  $1(0^-, 1)$  potentials. The accuracy of these potentials, however, is insufficient to predict the number of molecular bound states and thus of the exact location of Feshbach resonances. Joint experimental and theoretical efforts are required to determine these quantities.

Secondly, we computed rovibrationally averaged one- and two-photon transition dipole moments from one of the weakly bound 1(1)  $s$ -wave vibrational levels to the  $v = 0$ ,  $s$ -wave rovibrational level of the  $1(0^+)$  ground electronic state. We chose vibrational levels of the adiabatic  $3(0^+)$  state as intermediate levels and suggest that vibrational levels about  $hc \times 1600 \text{ cm}^{-1}$  above the minimum energy of the  $3(0^+)$  potential are the most favorable for FrAg formation. This suggestion also implies the need for very different laser frequencies for the STIRAP process.

In the future we hope to improve the quality of our predictions of the stimulated Raman and STIRAP transition strengths. In this article, we made several approximations to find initial order of magnitude estimates. The most problematic one might be the adiabatic approximation of the intermediate  $3(0^+)$  state. Non-adiabatic mixing near avoided crossings between the  $2(0^+)$  and  $3(0^+)$  states can be important.

### IV. ACKNOWLEDGMENTS

Work at Temple University is supported by the U.S. Air Force Office of Scientific Research Grants No. FA9550-21-1-0153 and No. FA9550-19-1-0272, the NSF Grant No. PHY-1908634. We thank Dr. D. DeMille, Dr. T. Fleig, and Dr. A. Petrov for fruitful discussions.

#### Appendix A: Electronic structure computations

We have performed Kramers unrestricted relativistic coupled-cluster calculations with single, double, and perturbative triplet excitations (CCSD(T)) [45] using

DIRAC program [32] for the ground  $n(\Omega^\sigma) = 1(0^+)$  and  $1(0^-)$  states of FrAg corresponding to the Hund's case (a) singlet  $X^1\Sigma^+$  state and the energetically lower of the two relativistic components of the triplet  $a^3\Sigma^+$  state, respectively. The small-core relativistic effective core potential, designed for the aug-cc-pwCV5Z-PP basis sets, from Ref. [46] has been used. In particular, we use the ECP78MDF and ECP28MDF core potentials for Fr and Ag, respectively. Reference molecular orbitals and determinants are obtained from relativistic Dirac-Coulomb Hartree-Fock calculations and only electrons in the outermost  $6s^2 6p^6 7s^1$  shells of Fr and  $4s^2 4p^6 4d^{10} 5s^1$  shells of Ag are correlated in the calculations.

We find that the  $1(0^+)$  ground state is well described by a single determinant near the repulsive wall and global minimum up to interatomic separations of  $\mathcal{R}_X = 11a_0$ . For separations between  $13a_0$  and  $14a_0$  the ground state energy has an unphysical maximum. Here, the  $1(0^+)$  potential is closest to that of the  $2(0^+)$  or  $A^1\Sigma^+$  state and its electronic wavefunction is multi-reference in nature. Consequently, the  $1(0^+)$  potential can only be used for  $R \leq \mathcal{R}_X$  and the molecular interaction energies must be obtained by subtracting the ground-state monomer energies of Fr and Ag obtained with the same Kramers unrestricted CCSD(T) method and basis sets. DIRAC calculations of the energies of the  $1(0^-)$  state do not suffer from unphysical maxima and we are able to use the results for  $R$  up to  $\mathcal{R}_a = 19a_0$ . We again subtract the ground-state monomer energies of Fr and Ag to determine the potential  $V_{1(0^-)}(R)$ .

Potential energies of other electronic states have been calculated within the Generalized Active Space (GAS) approach of relativistic four-component all-electron LUCIA calculations. Reference orbitals or spinors have been obtained from open-shell Dirac-Coulomb Hartree Fock calculations with two open shell orbitals, namely the  $7s$  orbital of Fr and the  $5s$  orbital of Ag. The remaining less-extended orbitals are kept doubly occupied. In the end the GAS approach has 58 inactive and 38 active spinor orbitals. Virtual unoccupied orbitals are build up from the atomic basis set.

Our choice of GAS allows for single excitations from the  $6p$  shell of Fr, single excitations from the  $4d$  shell of Ag, two excitations from the  $6p7s$  shell pair of Fr, as well as two excitations from the  $4d5s$  shell pair of Ag. To avoid so-called accidental root flipping, we request convergence of 10 roots or eigenstates for each  $\Omega$ .

The LUCIA calculations have been used to determine both potentials and  $R$ -dependent transition dipole mo-

ments. All  $\Omega = 0^+, 0^-, 1$  and  $2$  potentials dissociating to either the excited  $\text{Fr}(7p_{1/2})$  or  $\text{Fr}(7p_{3/2})$  limits while Ag remains in its ground state are shown in Fig. 9. In the main part of this paper a subset of these potentials, those relevant for STIRAP-based formation of the FrAg molecule, as well as relevant transition dipole moments have already been shown.

For the coupled-channels calculations we need as input potentials  $V_X(R)$  and  $V_a(R)$  for the Hund's case (a) non-relativistic singlet  $X^1\Sigma^+$  and triplet  $a^3\Sigma^+$  states, respectively. We can use  $V_X(R) \equiv V_{1(0^+)}(R)$  for the  $X^1\Sigma^+$  state from the CCSD(T) calculations. For potential of the triplet  $a^3\Sigma^+$  state, we must combine the data from the coupled-cluster and LUCIA calculations. Our CCSD(T) data are more accurate than those from LUCIA calculations. On the other hand coupled-cluster calculations and their extensions could not be used to determine the  $1(1)$  component of the  $a^3\Sigma^+$  state. Instead we construct a  $V_{1(1)}(R)$  potential by adding the small positive splitting  $V_{1(1)}(R) - V_{1(0^-)}(R)$  between the  $1(1)$  and  $1(0^-)$  states from the LUCIA calculations to the CCSD(T)  $V_{1(0^-)}(R)$  potential. It is worth noting that the small splitting is due to second-order spin-orbit effects with distant excited electronic states. Finally, we use that  $V_a(R) \equiv (V_{1(0^-)}(R) + 2V_{1(1)}(R))/3$ , a weighted mean or barycenter of the potentials for the two components of the  $a^3\Sigma^+$  state, based on an effective dipolar rank-2 spin-spin Hamiltonian between the electron spins of each of the atoms.

We realize that for separations, where the electron wavefunctions of the atoms barely overlap, *i.e.*  $R > \mathcal{R}_{\text{disp}} \approx 22a_0$ , both  $V_X(R)$  and  $V_a(R)$  approach the dispersion potential  $V_{\text{disp}}(R) = -C_6/R^6 - C_8/R^8$  omitting smaller contributions. The van-der-Waals dispersion coefficient  $C_6 = 1116E_h a_0^6$  was already computed in Ref. [31]. Currently, no value for the  $C_8$  dispersion coefficient is available. We chose  $C_8 = 746\,685E_h a_0^8$  inline with typical values for alkali-metal dimers and leading to a reasonable connection to the DIRAC results for the short-range potentials. We then connect each short-range DIRAC potential to the long-range dispersion potential using extrapolations of  $V_{X,a}(R)$  and  $V_{\text{disp}}(R)$  to intermediate-range where  $\mathcal{R}_i < R < \mathcal{R}_{\text{disp}}$ ,  $V_i^{\text{tot}}(R) = [1 - s(R; \vec{p})]V_i(R) + s(R; \vec{p})V_{\text{disp}}(R)$  for  $i = X$  and  $a$  and step-like functions  $s(R; \vec{p})$  with values between 0 and 1 for increasing  $R$ . Here,  $\vec{p}$  represents state-dependent adjustable parameters and  $s(R; \vec{p})$  is based on the trigonometric function  $\tanh(x)$ . We have verified that with this procedure  $V_X^{\text{tot}}(R)$  and  $V_a^{\text{tot}}(R)$  do not cross.

- 
- [1] I. Cirac and P. Zoller, *Physics Today* **57**, 38 (2004).  
 [2] D. Weiss and M. Saffman, *Physics Today* **70**, 44 (2017).  
 [3] A. D. Ludlow, M. M. Boyd, J. Ye, E. Peik, and P. O. Schmidt, *Rev. Mod. Phys.* **87**, 637 (2015).  
 [4] S. M. Brewer, J.-S. Chen, A. M. Hankin, E. R. Clements, C. W. Chou, D. J. Wineland, D. B. Hume, and D. R.

- Leibrandt, *Phys. Rev. Lett.* **123**, 033201 (2019).  
 [5] D. DeMille, *Phys. Rev. Lett.* **88**, 067901 (2002).  
 [6] K.-K. Ni, T. Rosenband, and D. D. Grimes, *Chem. Sci.* **9**, 6830 (2018).  
 [7] E. R. Hudson and W. C. Campbell, *Phys. Rev. A* **98**, 040302 (2018).



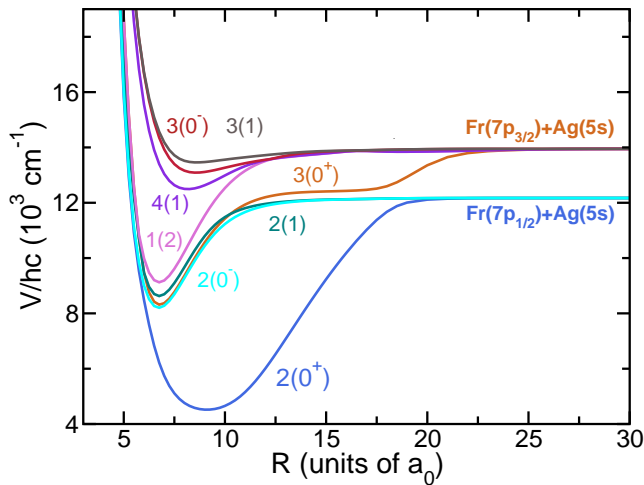


FIG. 9. Some relativistic electronic excited-state potentials of FrAg as functions of separation  $R$ . Potentials are identified by Hund's case (c) state labels  $n(\Omega^\sigma)$  and by atomic labels for large  $R$ . The zero of energy is at the dissociation limit or threshold of the ground electronic state.

- [8] E. A. Hinds, *Phys. Scr.* **T70**, 34 (1997).
- [9] M. S. Safronova, D. Budker, D. DeMille, D. F. J. Kimball, A. Derevianko, and C. W. Clark, *Rev. Mod. Phys.* **90**, 025008 (2018).
- [10] N. R. Hutzler, *Quantum Sci. Technol.* **5**, 044011 (2020).
- [11] O. P. Sushkov, V. V. Flambaum, and I. B. Khriplovich, *JETP* **60**, 873 (1984).
- [12] L. Skripnikov, N. Mosyagin, and V. V. F. A.V. Titov, *Phys. Chem. Chem. Phys.* **22**, 18374 (2020).
- [13] T. A. Isaev, S. Hoekstra, and R. Berger, *Phys. Rev. A* **82**, 052521 (2010).
- [14] T. A. Isaev, A. V. Zaitsevskii, and E. Eliav, *J. Phys. B* **50**, 225101 (2017).
- [15] A. D. Kudashov, A. N. Petrov, L. V. Skripnikov, N. S. Mosyagin, T. A. Isaev, R. Berger, and A. V. Titov, *Phys. Rev. A* **90**, 052513 (2014).
- [16] R. F. Garcia Ruiz, R. Berger, and et al., *Nature* **581**, 396–400 (2020).
- [17] P. Yu and N. R. Hutzler, *Phys. Rev. Lett.* **126**, 023003 (2021).
- [18] T. Fleig and D. DeMille, arXiv:2108.02809v1 (2021).
- [19] E. Gomez, S. Aubin, G. D. Sprouse, L. A. Orozco, and D. P. DeMille, *Phys. Rev. A* **75**, 033418 (2007).
- [20] M. Tandeci, J. Zhang, R. Collister, S. Aubin, J. A. Behr, E. Gomez, G. Gwinner, L. A. Orozco, and M. R. Pearson, *J. Instrum.* **8**, P12006 (2013).
- [21] V. V. Flambaum and I. B. Khriplovich, *JETP* **62**, 872 (1985).
- [22] D. P. DeMille, “Private communication,” (2021).
- [23] R. C. Bilodeau, M. Scheer, and H. K. Haugen, *J. Phys. B* **31**, 3885 (1998).
- [24] G. Uhlenberg, J. Dirscherl, and H. Walther, *Phys. Rev. A* **62**, 063404 (2000).
- [25] G. Herzberg, *Molecular Spectra and Molecular Structure*, 2nd ed. (Krieger Publishing Company, 1950).
- [26] E. E. Nikitin and R. N. Zare, *Mol. Phys.* **82**, 85 (1994).
- [27] K.-K. Ni, S. Ospelkaus, M. de Miranda, A. Pe'er, B. Neyenhuis, J. Zirbel, S. Kotochigova, P. Julienne, D. Jin, and J. Ye, *Science* **322**, 231 (2008).
- [28] S. A. Moses, J. P. Covey, M. T. Miecniowski, D. S. Jin, and J. Ye, *Nat. Phys.* **13**, 13 (2017).
- [29] C. Chin, R. Grimm, P. Julienne, and E. Tiesinga, *Rev. Mod. Phys.* **82**, 1225 (2010).
- [30] K. Bergmann, H. Theuer, and B. W. Shore, *Rev. Mod. Phys.* **70**, 1003 (1998).
- [31] M. Śmiałkowski and M. Tomza, *Phys. Rev. A* **103**, 022802 (2021).
- [32] DIRAC, a relativistic *ab-initio* electronic structure program, Release DIRAC21 (2021), written by R. Bast, A. S. P. Gomes, T. Saue, L. Visscher, and H. J. Aa. Jensen, (available at <http://dx.doi.org/10.5281/zenodo.4836496>, see also <http://www.diracprogram.org>).
- [33] O. Docenko, M. Tamanis, R. Ferber, H. Knöckel, and E. Tiemann, *Phys. Rev. A* **83**, 052519 (2011).
- [34] T. Takekoshi, M. Debatin, R. Rameshan, F. Ferlaino, R. Grimm, H.-C. Nägerl, C. R. Le Sueur, J. M. Hutson, P. S. Julienne, S. Kotochigova, and E. Tiemann, *Phys. Rev. A* **85**, 032506 (2012).
- [35] S. Sainis, J. Sage, E. Tiesinga, S. Kotochigova, T. Bergeman, and D. DeMille, *Phys. Rev. A* **86**, 022513 (2012).
- [36] H. T. C. Stoof, J. M. V. A. Koelman, and B. J. Verhaar, *Phys. Rev. B* **38**, 4688 (1988).
- [37] H. Dahmen and S. Penselin, *Z. Phys.* **200**, 456 (1967).
- [38] A. Coc, C. Thibault, F. Touchard, H. Duong, P. Juncar, S. Liberman, J. Pinard, J. Lermé, J. Vialle, S. Büttgenbach, A. Mueller, and A. Pesnelle, *Phys. Lett. B* **163**, 66 (1985).
- [39] C. Ekström, L. Robertsson, and A. Rosén, *Phys. Scr.* **34**, 624 (1986).
- [40] N. J. Stone, *Table of Nuclear Magnetic Dipole and Electric Quadrupole Moments* (International Atomic Energy Agency (IAEA), 2014) INDC(NDS)–0658.
- [41] W. Huang, M. Wang, F. Kondev, G. Audi, and S. Naimi, *Chinese Phys. C* **45**, 030002 (2021).
- [42] B. Gao, *Phys. Rev. A* **62**, 050702 (2000).
- [43] G. F. Gribakin and V. V. Flambaum, *Phys. Rev. A* **48**, 546 (1993).
- [44] S. Kotochigova, T. Zelevinsky, and J. Ye, *Phys. Rev. A* **79**, 012504 (2009).
- [45] L. Visscher, T. J. Lee, and K. G. Dyall, *The Journal of Chemical Physics* **105**, 8769 (1996).
- [46] M. Dolg and X. Cao, *Chem. Rev.* **112**, 403 (2012).